Nano Energy 108 (2023) 108239

Contents lists available at ScienceDirect

Nano Energy

journal homepage: www.elsevier.com/locate/nanoen

Self-powered triboelectric mechanical motion sensor for simultaneous monitoring of linear-rotary multi-motion

Xiaosong Zhang [a,b], Hengyu Li [a], Qi Gao [a,b], Zitang Yuan [a], Siyang He [a], Xin Yu [a], Zhong Lin Wang [a,c,*], Tinghai Cheng [a,b,*]

[a] Beijing Institute of Nanoenergy and Nanosystems, Chinese Academy of Sciences, Beijing 101400, China
[b] School of Nanoscience and Technology, University of Chinese Academy of Sciences, Beijing 100049, China
[c] Georgia Institute of Technology, Atlanta, GA 30332–0245, USA

ARTICLE INFO

Keywords:
Linear-rotary multi-motion
Simultaneous monitoring
Self-powered
Triboelectric mechanical motion sensor

ABSTRACT

To realize the simultaneous monitoring of linear-rotary multi-motion, a linear and rotary coupled-motion triboelectric mechanical motion sensor (LRC-TMMS) with a gear-like engagement electrode (GE-electrode) is proposed. The displacement and velocity measurement of the linear and rotary motions can be realized by using GE-electrode, and the linear, rotary, and helical motions of the LRC-TMMS can be distinguished by the signal processing method of fundamental frequency separation. The results illustrate that the LRC-TMMS can achieve stable monitoring with a maximum linear stroke of 70 mm. And the linear fitting lines between the parameters of the output signal and that of the input motion are consistent with the theoretical reference results. In addition, the velocities monitored by the LRC-TMMS in different motions have good linearity, and most error rates are less than 3%. The practical monitoring performance of the LRC-TMMS in nine motion modes is verified using a commercial linear-rotary motor, which has potential application prospects in the fields of the intelligent manipulator and automated manufacturing.

1. Introduction

Linear motion and rotary motion, as the most common modes of mechanical motion, are the widely used in various industries [1–4]. In particular, it is particularly necessary to use sensors to monitor the linear and rotary motions in typical scenarios such as the control of motors or reducers in industry, the positioning of drives, and the feedback of robot joint motion. To adapt to different usage requirements, the types of sensors that monitor linear motion [5,6] or rotary motion [7,8] are also diverse. It is worth mentioning that some sensors can be adapted for multi-degree-of-freedom motion monitoring, such as hall-effect sensors [9], optical sensors [10,11], accelerometers [12], etc. However, they all required multiple sensors to achieve simultaneous detection of the linear and rotary motions, which have the problems of large installation space and complex detection algorithms. For example, Lee et al. developed a sensing system that utilizes three optical sensors located at different locations to measure and control the attitude. And since the optical sensors need to maintain a measurement gap, it is equipped with multiple passive joints [10]. Onodera et al. proposed a motion sensor that can distinguish 6-DOF motion using six linear accelerometers [12]. Furthermore, the motion space of the traditional multi-motion sensing system is easily disturbed and the maintenance cost is high, due to the power supply and wiring issues. Therefore, self-powered sensing technology has become a new trend in the development of motion sensors [13–15].

In 2012, Wang's group invented the triboelectric nanogenerator (TENG) for the first time based on triboelectric and electrostatic induction effects [16], which can be used for micro/nano energy harvesting [17–19] and self-powered sensing [20,21]. As a novel self-powered sensing technology, TENG has the advantages of multi-form and low-cost [22,23], which has shown broad application prospects in mechanical motion monitoring [24–26], fluid sensing [27,28], exercise/health monitoring [29,30], and intelligent facilities [31,32]. Especially for linear and rotary motions, researchers have proposed a variety of representative triboelectric mechanical motion sensors [33–35], and also designed some sensors that can monitor linear motion as well as rotary motion [36,37]. It is noted that these sensors can only achieve step-by-step monitoring of one motion form (linear motion or

* Corresponding authors at: Beijing Institute of Nanoenergy and Nanosystems, Chinese Academy of Sciences, Beijing 101400, China
E-mail addresses: zhong.wang@mse.gatech.edu (Z.L. Wang), chengtinghai@binn.cas.cn (T. Cheng).

https://doi.org/10.1016/j.nanoen.2023.108239
Received 9 December 2022; Received in revised form 8 January 2023; Accepted 27 January 2023
Available online 2 February 2023

rotary motion) at a time. There is no triboelectric mechanical motion sensor that can simultaneously monitor linear-rotary multi-motion.

Herein, a linear and rotary coupled-motion triboelectric mechanical motion sensor (LRC-TMMS) for multi-motion simultaneous monitoring is proposed. The LRC-TMMS uses a gear-like engagement electrode (GE-electrode) to generate two voltage signals with large amplitude differences in the linear and rotary motions. After signal processing, the LRC-TMMS can realize simultaneous monitoring of linear-rotary multi-motion. Firstly, the operating principle of the LRC-TMMS is analyzed. The prototype of the LRC-TMMS is developed and the experimental system is built. Subsequently, the displacement monitoring performance of the LRC-TMMS is explored, and the output signals of the LRC-TMMS under linear, rotary and helical motions with different velocities are also measured. In addition, the linear relationship and error rate between the signal frequency and the input velocity are analyzed. Finally, the demonstrations and durability experiments are carried out, which prove the feasibility of the LRC-TMMS in practical applications of the intelligent robot, manipulator, capping machine and semiconductor packaging.

2. Results and discussion

2.1. Structural design and operating principle

Based on the triboelectric and electrostatic induction effects, the amplitude of the voltage signal generated by the sliding contact of two friction materials with different triboelectric polarities is positively correlated with the contact area and has nothing to do with the frequency. Therefore, a special GE-electrode is designed on the basis of above mentioned characteristics, as sketched in Fig. 1a. Rectangular electrodes with different areas are staggered and connected to the centerline of the electrode to form an electrode. Multiple electrodes are arranged in parallel and engaged with each other to form the GE-electrode.

The LRC-TMMS consists of a stator, a mover, and a pair of GE-electrodes, and the assembly process is illustrated in Fig. 1b. The copper electrodes of the designed GE-electrode are mounted on the inner surface of the cylindrical stator. The PTFE films are evenly distributed and circumferentially mounted on the outer surface of the mover. Through the linear and rotary movements of the mover, the PTFE films and the copper electrodes generate relative motion, thereby monitoring the motion status of the linear and rotary direction. The LRC-TMMS converts the external mechanical energy of the linear and rotary motions into electricity based on the triboelectric and electrostatic induction effects. Fig. 1c illustrates the prototype photographs of the LRC-TMMS. The length and diameter of both ends of the mover can be determined according to the actual working state. A more detailed description is given in the experimental section.

The copper electrodes and PTFE film constitute the electromechanical conversion part of the LRC-TMMS. According to Fig. 2a, the electromechanical conversion principle of the LRC-TMMS is illustrated. When the mover moves linearly in the stator (Fig. 2a(i)), the surfaces of the copper electrode and PTFE films will produce the same amount of charges of opposite nature due to the different triboelectric polarities. When the PTFE films on the mover completely correspond to the copper-1 on the GE-electrode, the positive charge of the copper-1 is equal to the negative charge on the surface of the PTFE film. At this time, copper-1 and copper-2 of GE-electrode are in electrostatic balance. When the PTFE films slide from the corresponding position on copper-1 to copper-2, the original electrostatic balance will be destroyed. Under the action of electrostatic induction, there will be a potential difference between copper-1 and copper-2, which will transfer electrons from copper-2 to copper-1 to form a new electrostatic balance and make the external load form a current. Finally, when the PTFE films completely overlap with copper-1 at the next position, the electrostatic balance between the electrodes will be reached again. And the electrons will be transferred to copper-2 again to make the external load form a current in the opposite direction. This is the complete process of generating a periodic electrical signal. And when the mover is in continuous motion, it causes the LRC-

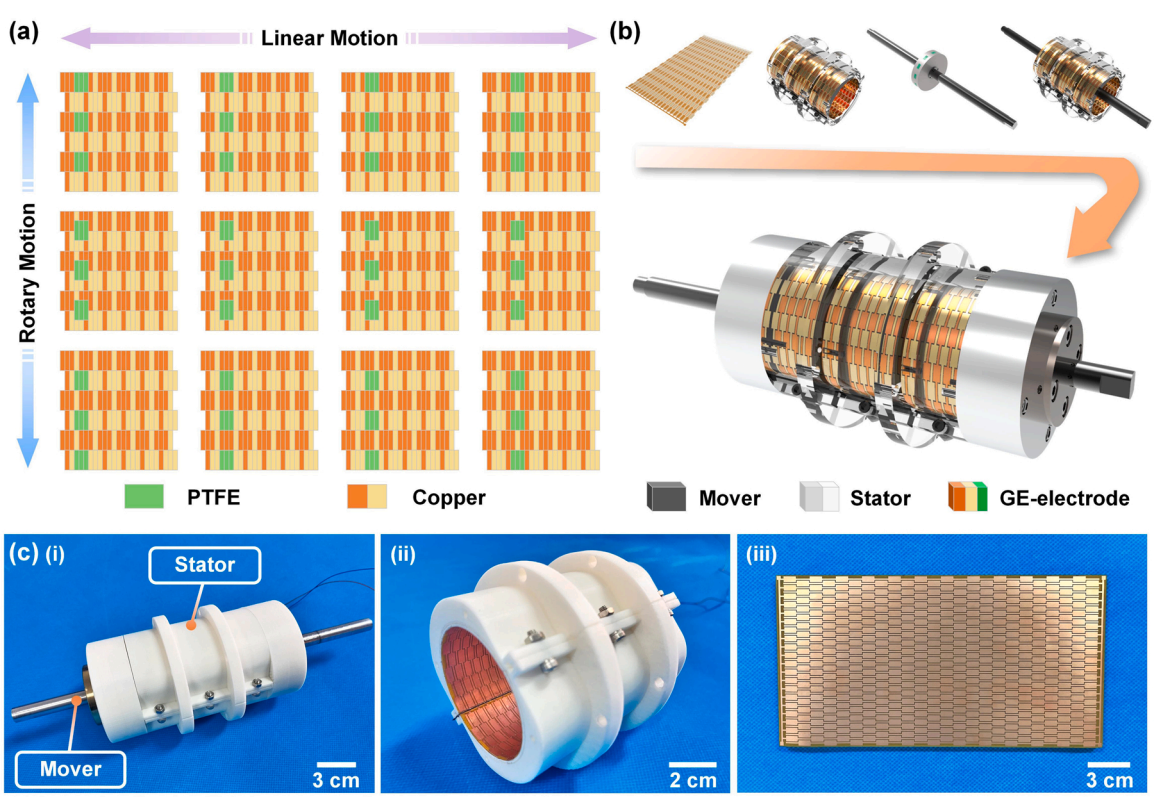

Fig. 1. Structural design of the LRC-TMMS. (a) GE-electrode structure. (b) Assembly process and schematic structure. (c) Photographs of the prototype.

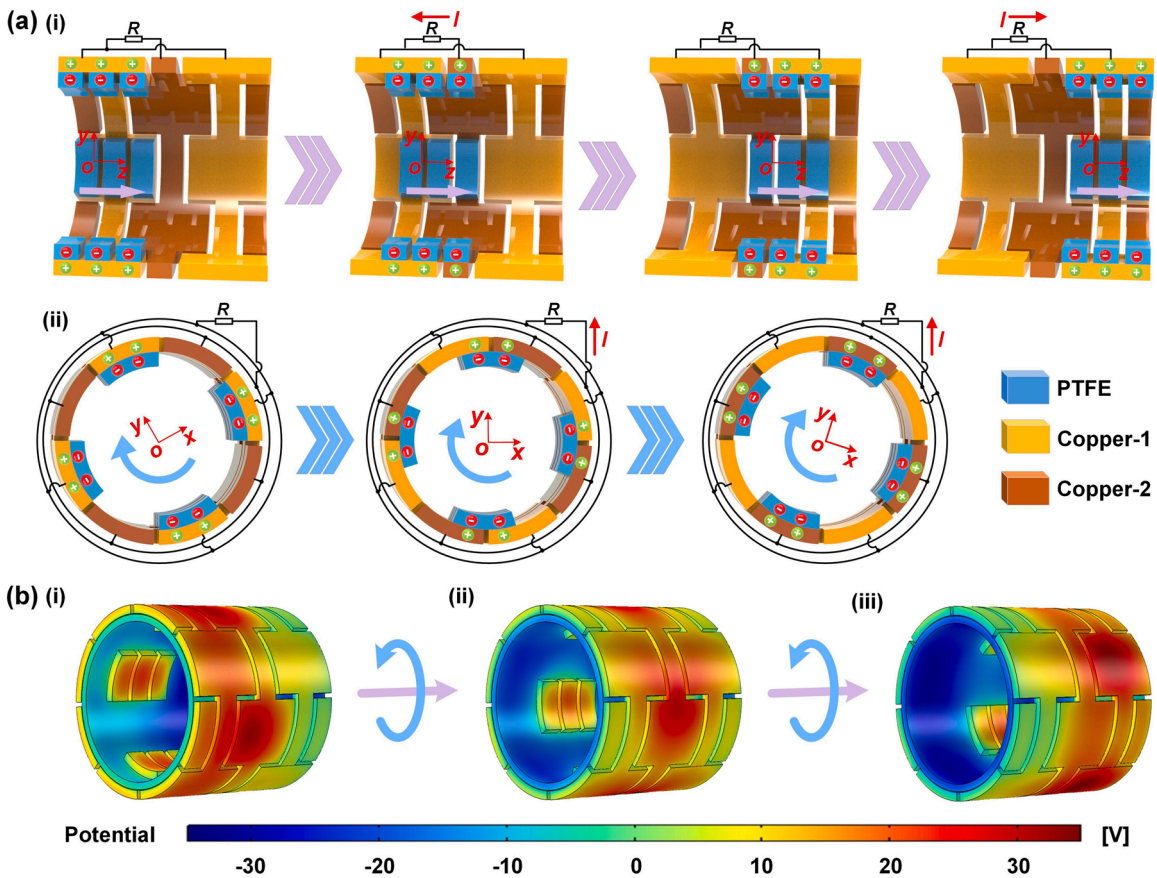

Fig. 2. Operating principle analysis of the LRC-TMMS. (a) Charge transfer process under (i) linear motion and (ii) rotary motion. (b) Potential distribution simulation under helical motion.

TMMS to generate an alternating current (AC) signal. Similarly, a similar charge transfer process occurs on the GE-electrode when the mover rotates in the stator (Fig. 2a(ii)).

Due to the smaller size of the electrode, metal processing is simpler than that of PTFE film. Therefore, the inner surface of the PTFE film is affixed with a metal of the corresponding shape. Fig. 2b describes the helical motion process of the LRC-TMMS and the numerical simulation of the electrostatic field in the case of the open circuit by COMSOL software. Only the PTFE films corresponding to the metal electrode of the mover acts on the copper electrodes of the stator. The electrostatic induction effect of the excess part on the PTFE films and the copper electrodes of stator can be canceled out. Therefore, when the metal electrode on the mover moves helically, the stator copper electrodes corresponding to the moving metal electrode presents the highest positive potential. And with the motion of the metal electrode, the position of the highest positive potential on the stator copper electrode changes, causing the potentials of the two copper electrodes on the stator to change with each other, thereby generating an AC signal. Comparing the simulation results with the charge transfer process in Fig. 2a can further enhance the elaboration of the sensing signal generation mechanism of the LRC-TMMS.

2.2. Model analysis and signal processing

According to the operating principle of the LRC-TMMS, a theoretical model of sliding freestanding triboelectric-layer nanogenerator is established, as shown in Fig. 3a. When the sensor performs linear and rotary coupled-motion at the same time, the output voltage signal $g(t)$ is composed of two fundamental frequency signals and noise, and its expression is:

$$g(t) = g_1(t) + g_2(t) + g_{\mathrm{Noise}}(t) \tag{1}$$

Among them, the output signal of LRC-TMMS is similar to a sinusoidal signal. The fundamental frequency signal can be expressed as:

$$g_n(t) = A_n \sin(\omega_n t + \varphi_n) \tag{2}$$

where A_n is the amplitude of the signal, ω_n is the angular frequency, and φ_n is the initial phase. According to Fig. 3a and Eq. (S1 – S6), the amplitude of the signal is:

$$A_n = \frac{\sigma w l S_n}{C_0 S_0} \tag{3}$$

where σ is the charge density, w is the width of PTFE, l is the length of PTFE, C_0 is the capacitance between the two electrodes of the stator, S_0 is the area of the initial electrode, and S_n is the area of the next adjacent electrode of the mover in the moving direction.

It can be seen from Fig. 1a that when the mover produces the linear and rotary motions, the electrode area difference in the two vertical directions is different. When the LRC-TMMS performs a helical motion, the initial position of the PTFE is the same. Thus, it can be considered that S_0 in the two directions is the same, and the S_n is different. Therefore, where $n = 1, 2$. Among them, $S_0 > S_n$. And the expression for frequency is:

$$f_n = \frac{\omega_n}{2\pi} \tag{4}$$

So, Eq. (1) can be expressed as:

$$g(t) = \frac{\sigma w l}{C_0 S_0}[S_1 \sin(2\pi f_1 t + \varphi_1) + S_2 \sin(2\pi f_2 t + \varphi_2)] + g_{\mathrm{noise}}(t) \tag{5}$$

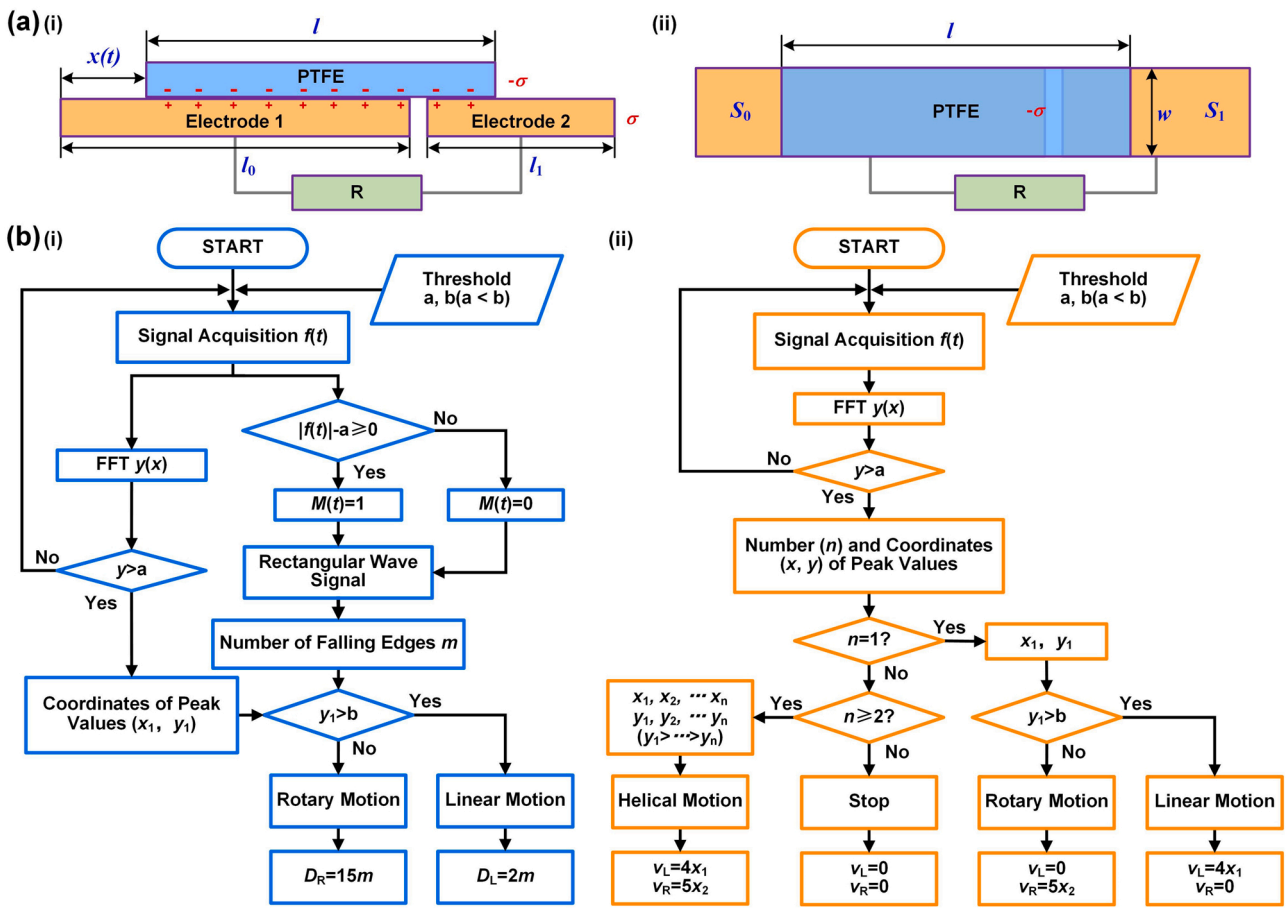

Fig. 3. Theoretical modeling and signal processing of the LRC-TMMS. (a) Theoretical model. (b) Signal processing flow of (i) displacement and (ii) velocity.

Among them, the areas of S_1 and S_2 are not equal. Therefore, by performing fast Fourier transform (FFT) processing on the sampled signal $g(t)$, two fundamental frequency signals with different amplitudes can be extracted as motion information in two directions. The above model is verified by MATLAB software analog signal extraction (Fig. S1 and Table S1).

As shown in Fig. 3b, through signal processing and analysis, the LRC-TMMS can realize the displacement or velocity simultaneous monitoring of multi-motion. In this paper, the displacement resolution of linear motion is 2 mm and the angle resolution of rotary motion is 15°. A more detailed description is given in the Supporting Information.

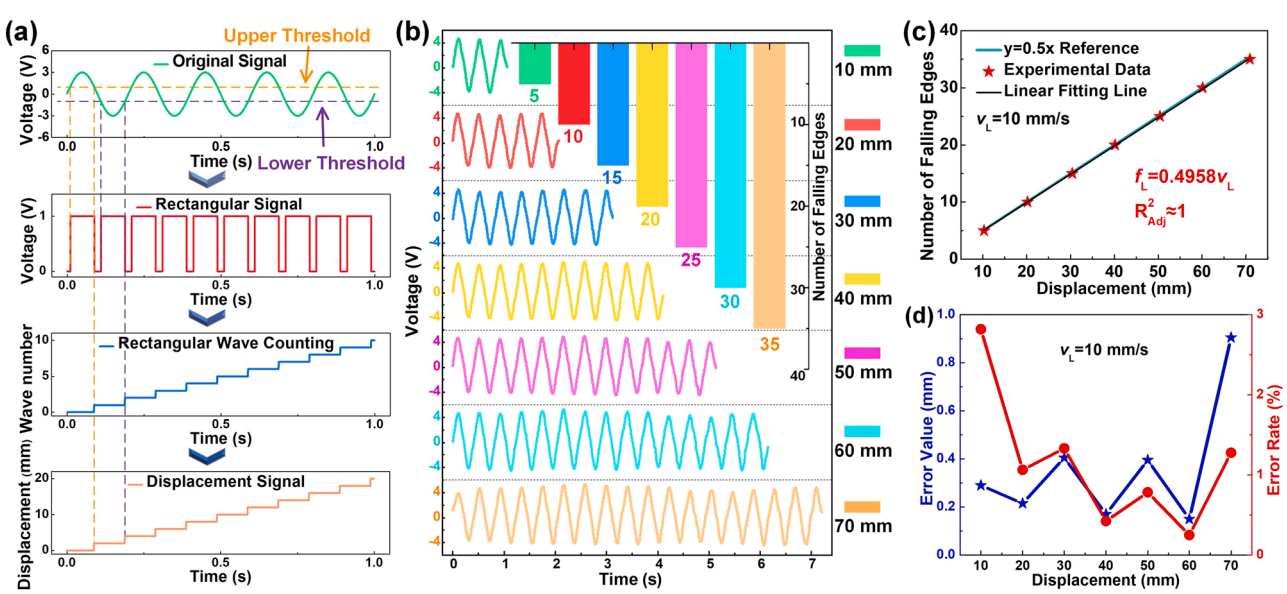

Fig. 4. Displacement monitoring performance. (a) Displacement calculation process. (b) Voltage curve. (c) Relationship between linear displacement and the number of falling edges. (d) Errors under different linear displacements.

2.3. Basic sensing performance

An experimental system (Fig. S2) that can realize multi-motion excitation of linear, rotary and helical motions is established to measure the basic performance of the LRC-TMMS. The results measured by commercial sensors are used as the calibration parameters to illustrate the sensing performance of the LRC-TMMS. A more detailed description is given in the experimental section. The displacement calculation process of the LRC-TMMS is illustrated in Fig. 4a. The original signal is converted into a rectangular wave signal through the thresholds, and the number of falling edges is counted to calculate the output displacement. Besides, the velocity can be calculated through the fundamental frequency obtained by the output voltage of the LRC-TMMS based on Fig. 3b.

Firstly, the output signals of the LRC-TMMS under different linear displacements are analyzed. The output voltages under different displacements between 10 and 70 mm are measured. As shown in Fig. 4b, the LRC-TMMS can output a stable AC signal under different linear displacements. And the number of falling edges of rectangular waves can be accurately obtained by signal processing. Meanwhile, the linear motion parameters are calculated through the output signals of the LRC-TMMS, in which the LRC-TMMS are calibrated by the values measured by the commercial displacement sensor, and the linearity and error rate at different linear displacements can be obtained. As shown in Fig. 4c, the number of falling edges has a good linear relationship with linear displacement, and the adjusted R-square is 0.9999. The linear fitting line is almost identical to the theoretical reference result. In addition, the error value and error rate of the sensor can be calculated by Eq. (S13) and Eq. (S14). The maximum error rate of the displacement measured by the LRC-TMMS is less than 3% in the maximum displacement of 70 mm, as sketched in Fig. 4d. The error fluctuation within a small range may be caused by random errors from the external environment and the device circuit. The above experiments prove the feasibility of the LRC-TMMS in displacement monitoring.

The velocity monitoring performance of the prototype is explained by analyzing the output signals of the LRC-TMMS in different motion modes. The output voltages of the LRC-TMMS under the different velocities of the linear and rotary motions are measured, respectively. The results show that the output voltage curves of the LRC-TMMS are stable under the linear velocity of 5 – 200 mm/s (Fig. 5a and S3a) or the rotary velocity of 20 – 200 rpm (Fig. 5d and S3b). And the voltage amplitude of the rotary motion is significantly lower than that of the linear motion, which further verifies the correctness of the theoretical model. To calibrate the velocity sensing characteristics of the LRC-TMMS, fundamental frequencies at different velocities are extracted to fit the straight line and compared with the theoretical reference result converted from Fig. 3b. As shown in Fig. 5b and e, there is a good linear relationship between the output signal frequency and the input velocity, which could be linearly fitted with the adjusted R-square of 0.9999 and about 1, respectively. It can be seen that although the errors occur during the measurement due to prototype assembly and motor input characteristics, the linear fitting line is almost identical to the theoretical reference result. Therefore, the correctness of the signal processing in Fig. 3b is verified, which is the basis for the LRC-TMMS as a velocity sensor. The deviation between the linear fitting line and the theoretical reference result is due to the measuring error of the LRC-TMMS. Therefore, the error values and the corresponding error rates are calculated under different velocities. As shown in Fig. 5c, the error value increases with the linear velocity, and the error rate of the LRC-TMMS is mostly below 3.5% in the linear velocity range of 5–200 mm/s. The more frequency components of variable motion mixed in, the interference to the main frequency of the extracted signal is increased. And the linear motor has variable motion during the start and the stop phases. Therefore, the faster the motion velocity, the shorter the time for the uniform motion of the mover, and the more other velocity components. Combined with the above reasons, the error values of linear velocity show an increasing trend. Moreover, the calibration results of the rotary velocity measured by the LRC-TMMS and the commercial encoder is illustrated in Fig. 5f. Since the voltage signal of rotary motion is extracted when the LRC-TMMS is in stable motion, the error values only fluctuate within a certain range, which is different from the trend of linear motion. And the maximum error rate of the LRC-TMMS is less than 0.4%. In addition, the velocity monitoring performance of the LRC-TMMS under different linear displacements is measured. As shown in Fig. S4, most error rates can be kept below 3%. A more detailed description is given in the Supporting Information.

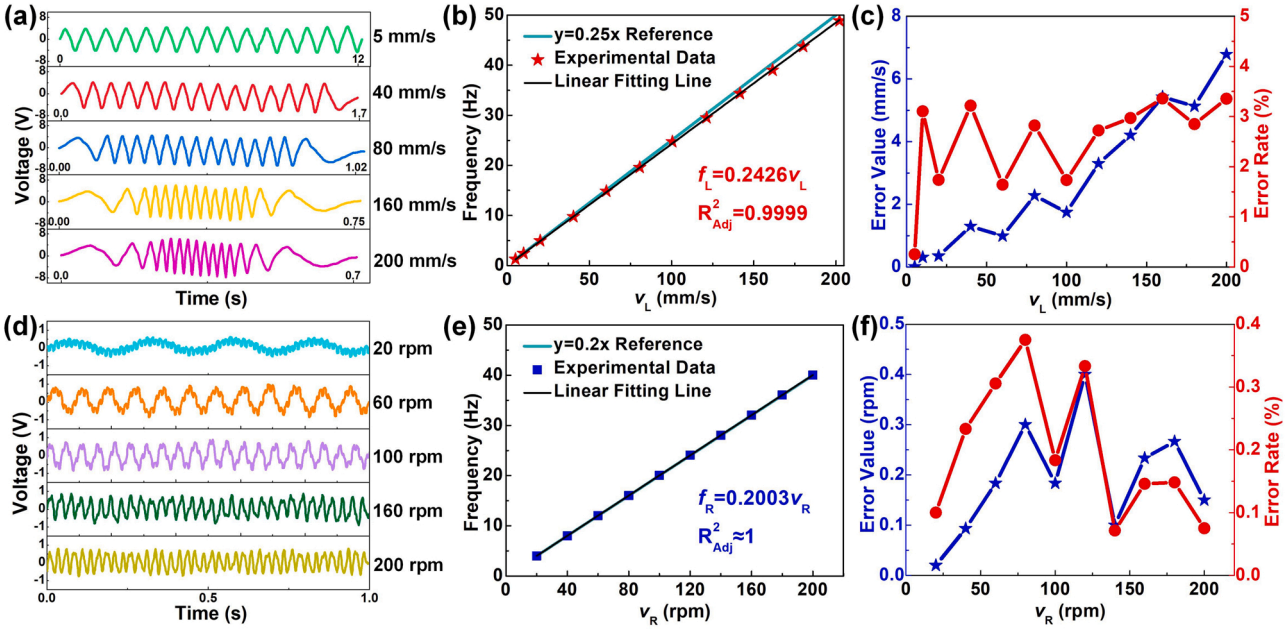

Fig. 5. Velocity monitoring performance. (a) Voltage curves under different linear velocities. (b) Relationship between linear velocity and signal frequency. (c) Errors under different linear velocities. (d) Voltage curves under different rotary velocities. (e) Relationship between rotary velocity and signal frequency. (f) Errors under different rotary velocities.

To prove that the LRC-TMMS can achieve the simultaneous monitoring of linear-rotary multi-motion, the sensing performance of the LRC-TMMS is measured under helical motion with a combination of the linear and rotary motions. Firstly, the output signals of the LRC-TMMS under rotary velocity with 100 rpm, linear motion with 60 mm stroke and different linear velocities are measured (Fig. S5a). The spectral analysis results of FFT processing of the output voltage are shown in Fig. 6a. Although there is a lot of noise, the two fundamental frequencies can be accurately identified. The signal frequency of the LRC-TMMS corresponding to the linear and rotary motions at different velocities can be extracted respectively, and the effects of the linear and rotary velocities on the signal frequency of helical motion can be obtained. As shown in Fig. 6b, the signal frequency of the LRC-TMMS corresponding to the fixed rotary velocity fluctuates near the reference line of the theoretical value of 20 Hz. The signal frequency of the LRC-TMMS corresponding to the variable linear velocity is linearly related to the adjusted R-square of 0.9987, and its linear fitting line is the same as the theoretical reference result. The error rate is calculated by the LRC-TMMS and commercial sensors, the results are shown in Fig. 6c. The most error rate of the linear and rotary motions is less than 3%. In addition, to represent the ability of the LRC-TMMS to detect fundamental frequency signals, the signal-to-noise ratio (SNR) of the LRC-TMMS is calculated based on the spectral analysis results of Fig. 6a. As shown in Fig. 6d, the maximum SNR of the linear and rotary motions can reach 28.22 dB and 20.14 dB, respectively. The SNR of linear motion is generally greater than that of rotary motion because the voltage amplitude of linear motion is greater than that of rotary motion.

Besides, the output signals of the LRC-TMMS under helical motion

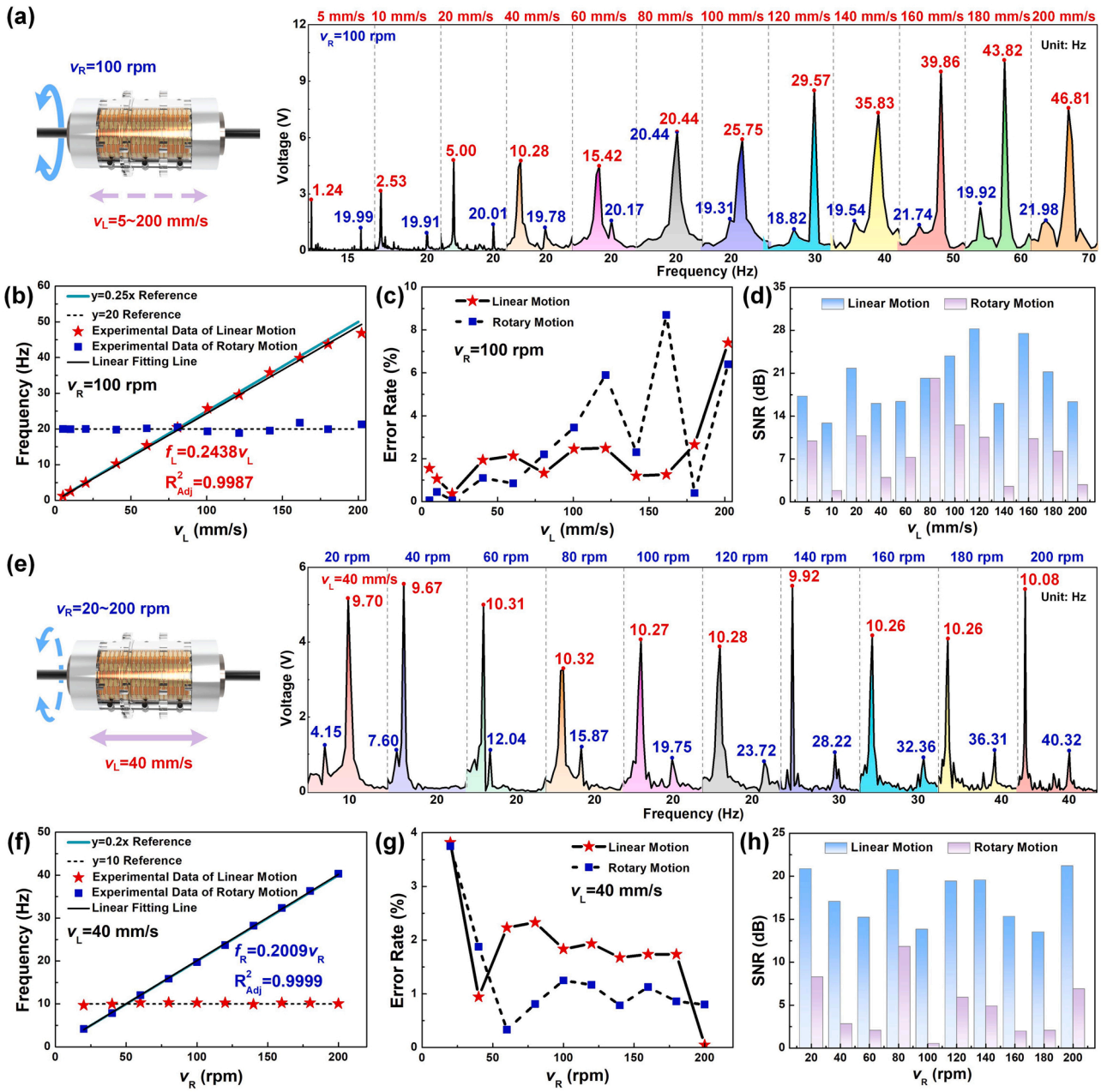

Fig. 6. Monitoring performance of helical motion. (a) Spectrum analysis results under 100 rpm and variable linear velocities. (b) Relationships between linear velocity and two signal frequencies. (c) Error rates under 100 rpm and variable linear velocities. (d) SNR under 100 rpm and variable linear velocities. (e) Spectrum analysis results under 40 mm/s and variable rotary velocities. (f) Relationships between rotary velocity and two signal frequencies. (g) Error rates under 40 mm/s and variable rotary velocities. (h) SNR under 40 mm/s and variable rotary velocities.

with different rotary velocities are measured, in which the linear stroke and velocity are 60 mm and 40 mm/s (Fig. S5b). The frequency spectrum of the output voltage is illustrated in Fig. 6e. Similarly, the two fundamental frequencies can be accurately extracted according to the amplitude of the voltage. Furthermore, the sensing performance of the LRC-TMMS is analyzed. As shown in Fig. 6 f, the extraction frequencies of the signals have expressed linearity with the rotary velocity, among which the adjusted R-square of the rotary motion is equal to 0.9999. And the signal frequency of the LRC-TMMS corresponding to the fixed linear velocity fluctuates near the reference line of the theoretical value of 10 Hz. As shown in Fig. 6 g, the most error rate of linear motion is also below 2.5%, and the most error rate of rotary motion is kept below 2%. In addition, the SNR of the linear and rotary motions can reach 20.86 dB and 11.82 dB, respectively. The results show that the LRC-TMMS can simultaneously monitor the linear and rotary velocity components of the helical motion.

3. Demonstration

The above sensing performance indicates that the LRC-TMMS is suitable for the monitoring of multiple mechanical motions such as linear, rotary and helical motion, individually or in combination, as shown in Table 1. The developed LRC-TMMS has potential application prospects in the intelligent robot, manipulator, capping machine and semiconductor packaging (Fig. 7a).

To explain the stability of LRC-TMMS as a monitoring sensor of multi-motion states, a commercial linear-rotary motor (LinMot, PR-52) is adopted to realize both linear and rotary motions, and is currently used in industries such as automated machinery and semiconductor manufacturing in Fig. 7a. The demonstration system of the LRC-TMMS is illustrated in Fig. 7b. The commercial motor is installed above the LRC-TMMS to generate linear, rotary, and helical motions. The demonstration program corresponding to the signal processing flow of Fig. 3b is written using LabVIEW software. The program can process and display the multi-motion states in real time, including the linear and rotary displacements (Fig. 7c(i)), and the velocity of linear, rotary, and helical motions (Fig. 7c(ii)). (Details are presented in Supporting Movie S1 and S2). The period of FFT in real-time processing is an important factor affecting the dynamic characteristics of the system. Taking the linear motion of 10 mm/s as an example, the sampling periods of 0.5 s and 1 s are set for comparison. As shown in Fig. 7d, the longer the sampling period, the smaller the real-time velocity error obtained. However, if the sampling period is increased, the tracking performance toward the velocity changed dynamically will deteriorate. Therefore, the sampling period of the system should be as short as possible under the premise of ensuring controllable error.

Supplementary material related to this article can be found online at doi:10.1016/j.nanoen.2023.108239.

The durability experiment of the LRC-TMMS is carried out using the demonstration system. The LRC-TMMS can still accurately extract the two fundamental frequencies corresponding to the linear and rotary motions after 17.5 h of continuous helical motion under the rotary velocity of 60 rpm, the stroke of 60 mm, and the linear velocity of 10 mm/s. As shown in Figs. S6 and 7e, the error rate of the LRC-TMMS always remains below 3%, and the error rate of rotary frequency is even below 1%, which proves that the LRC-TMMS is stable enough and has the potential for industrialization.

Table 1
Monitorable motion modes of the LRC-TMMS.

	Stop	Upward	Downward
Stop	Stop	Upward	Downward
Clockwise	Clockwise	Left-handed helix	Right-handed helix
Counterclockwise	Counterclockwise	Right-handed helix	Left-handed helix

4. Conclusion

In summary, a novel LRC-TMMS with a GE-electrode was proposed according to the positive correlation between the contact area and the amplitude of the output voltage of TENG. The operating principle of the LRC-TMMS was analyzed; the theoretical model was established and verified; the signal processing flow was also explained in detail. The sensing performance of the LRC-TMMS under linear, rotary, and helical motions has been measured, respectively. The linear and rotary displacement resolutions are 2 mm and 15°. Experimental results showed that the LRC-TMMS could stably monitor the motion displacement of the mover through the rectangular wave counting method, and the maximum linear stroke of the LRC-TMMS was 70 mm. Furthermore, the LRC-TMMS had good linearity under different motions, and most error rates were less than 3%. Finally, a commercial linear-rotary motor was used to demonstrate the practical application of the LRC-TMMS. And after 17.5 h of continuous helical motion, the error rate of the LRC-TMMS remained below 3%. Compared with the current multi-motion sensing systems, the LRC-TMMS can avoid the use of external power sources, so it is expected to realize self-powered sensing. In addition, since this monitor method only utilizes one sensor, it has the advantages of high integration and small installation space. This application of self-powered sensors will promote the development of mechanical motion monitoring technology.

5. Experimental section

5.1. Fabrication of the LRC-TMMS

The LRC-TMMS has dimensions of 66 mm (diameter) × 140 mm (length). The mover is made of aluminum alloy (AL7075). The stator is made by three-dimension printing (3DP) technology. A linear bearing is installed at each end of the stator to better transmit the linear and rotary motions, and then the mover passes through the linear bearings at both ends. Besides, to ensure full contact between the stator and mover, foam rubber (thickness 1 mm) is installed on the inner surface of the cylindrical stator, and then the copper electrode of GE-electrode is pasted on the foam rubber. The GE-electrode is made of the copper electrode layer (thickness 35 μm) and polyimide substrate (thickness 25 μm) through flexible printed circuit (FPC) technology. Among them, the copper electrode layer is designed with interconnected large rectangular electrodes (length 6 mm, width 2.8 mm) and small rectangular electrodes (length 6.4 mm, width 0.8 mm), and the gap between each column of electrodes is 0.2 mm. Because the output is set directly on the front of the GE-electrode, the FPC layer number is a single layer and there is no through-hole. The thickness of the PTFE film on the mover is 80 μm.

5.2. Measurement

The linear motor (QRXQ, RXP60–800) is installed on the workbench, and the rotary motor (Mitsubishi Electric, HG-KR43J) is installed on the moving platform of linear motor. The prototype is installed above the linear motor through the profile frame, and the mover of the prototype is connected to the rotary motor. The rotary motor matching encoder is installed at the rear end of the rotary motor for monitoring the rotary motion. The displacement sensor (Micro-Epsilon, ILD 1402–200) is installed on one side of the linear motor to monitor the linear motion. In addition, the measurement and acquisition of the output signal generated by the LRC-TMMS are realized by the data acquisition (DAQ) card (NI, USB-6218) and LabVIEW software.

CRediT authorship contribution statement

Xiaosong Zhang: Conceptualization, Investigation, Writing –

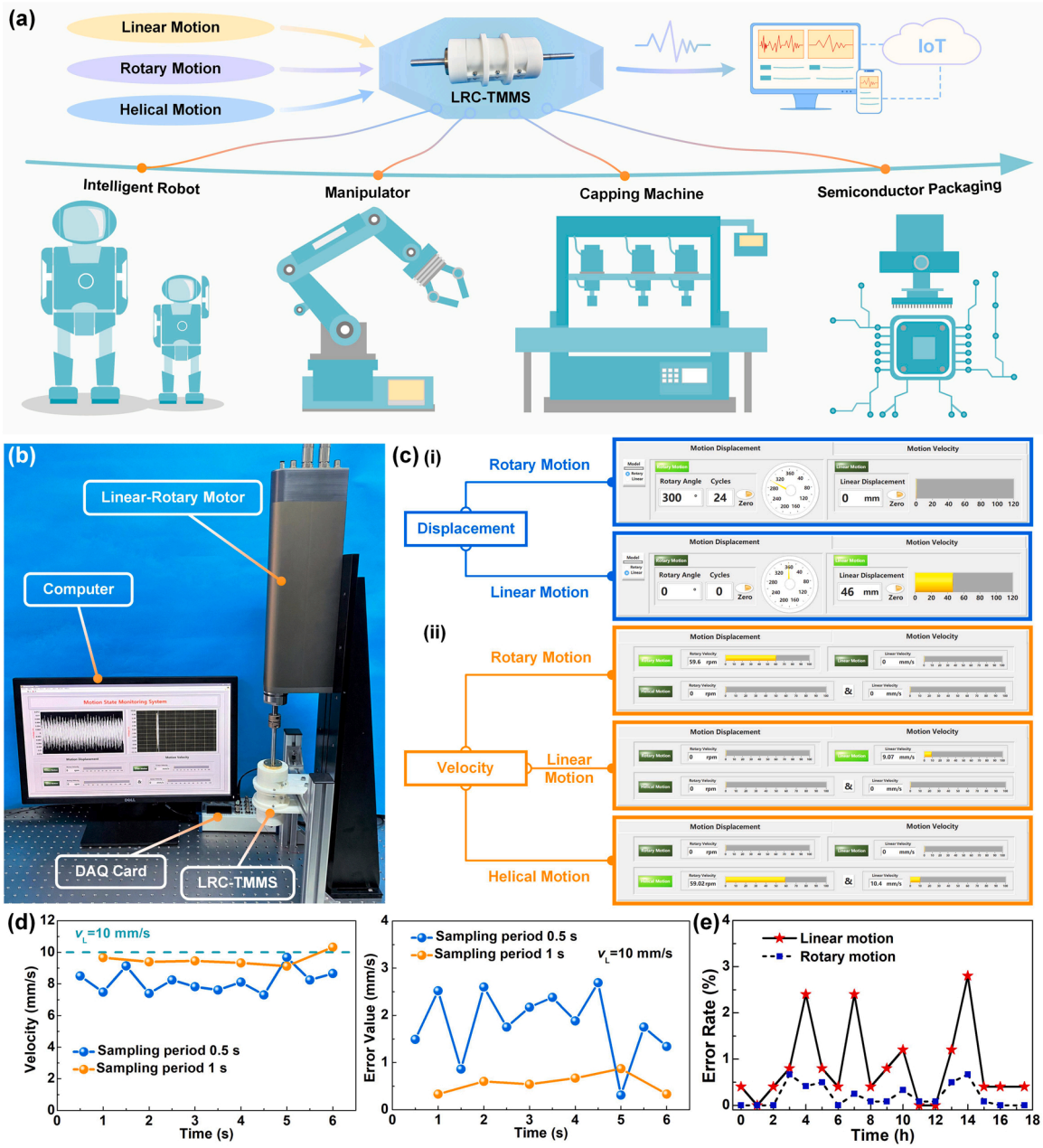

Fig. 7. Real-time motion state monitoring system based on the LRC-TMMS. (a) Application scenario. (b) Demonstration system. (c) Monitoring interfaces of displacement and velocity. (d) Real-time velocity and error value under different sampling periods. (e) Error rate of durability experiment.

original draft. **Hengyu Li:** Investigation, Writing – original draft. **Qi Gao:** Investigation, Validation. **Zitang Yuan:** Investigation. **Siyang He:** Investigation. **Xin Yu:** Investigation. **Zhong Lin Wang:** Conceptualization, Resources, Writing – review & editing, Supervision. **Tinghai Cheng:** Conceptualization, Resources, Writing – review & editing, Supervision.

Declaration of Competing Interest

The authors declare that they have no known competing financial interests or personal relationships that could have appeared to influence the work reported in this paper.

Data availability

Data will be made available on request.

Acknowledgments

The authors are grateful for the support received from the National Key R & D Project from the Minister of Science and Technology (Nos. 2021YFA1201601 and 2021YFA1201604).

Appendix A. Supporting information

Supplementary data associated with this article can be found in the online version at doi:10.1016/j.nanoen.2023.108239.

References

[1] T. Liu, F. Pagliano, R. Van Veldhoven, V. Pogoretskiy, Y. Jiao, A. Fiore, Integrated nano-optomechanical displacement sensor with ultrawide optical bandwidth, Nat. Commun. 11 (2020) 2407.

[2] Y. Lee, S.G. Kang, J. Jeong, A self-powered absolute shaft encoder based on triboelectric nanogenerator, Nano Energy 98 (2022), 107230.
[3] B. Rouzbeh, G. Bone, G. Ashby, High-accuracy position control of a rotary pneumatic actuator, IEEE/ASME Trans. Mech. 23 (2018) 2774–2781.
[4] Y. Hu, S. Zhang, Y. Yan, L. Wang, X. Qian, L. Yang, A smart electrostatic sensor for online condition monitoring of power transmission belts, IEEE Trans. Ind. Electron. 64 (2017) 7313–7322.
[5] J. Sun, C. Tian, T. Jiao, CPLD-based displacement measurement system for nanoscale grating ruler, J. Chem. 2020 (2020) 1–8.
[6] A. Jorgensen, S. Munk-Nielsen, C. Uhrenfeldt, Evaluation of in situ Thermomechanical Stress–Strain in Power Modules Using Laser Displacement Sensors, IEEE Trans. Power Electr. 36 (2021) 9411–9418.
[7] T. Tameh, M. Sawan, R. Kashyap, Smart integrated optical rotation sensor incorporating a fly-by-wire control system, IEEE Trans. Ind. Electron. 65 (2018) 6505–6514.
[8] N. Hagiwara, Y. Suzuki, H. Murase, A method of improving the resolution and accuracy of rotary encoders using a code compensation technique, IEEE Trans. Instrum. Meas. 41 (1992) 98–101.
[9] Y. Kawato, W.-J. Kim, A novel multi-dof precision positioning methodology using two-axis hall-effect sensors, Proc. 2005, Am. Control Conf. 5 (2005) 3042–3047.
[10] S.-M. Lee, H. Son, Multi-sensor integration and fusion for control of Multi-DOF spherical motion platform, Mechatronics 77 (2021), 102593.
[11] Y.-K. Kim, K.-S. Kim, S. Kim, Algorithm of markerless long distance 6-DOF motion detection system based on laser distance sensors, 2013 IEEE/ASME Int. Conf. Adv. Intell. Mechatron. (2013).
[12] R. Onodera, N. Mimura, Stability and error analysis of a new 6 dof motion sensor using multiple accelerometers, in: Sensors, 2007, IEEE, 2007, pp. 752–755.
[13] Q. Liu, X. Wang, W. Song, H. Qiu, J. Zhang, Z. Fan, M. Yu, Y. Long, Wireless single-electrode self-powered piezoelectric sensor for monitoring, ACS Appl. Mater. Interfaces 12 (2020) 8288–8295.
[14] W. Qiao, L. Zhou, Z. Zhao, D. Liu, S. Li, J. An, X. Li, Y. Gao, P. Yang, J. Liu, Z. L. Wang, J. Wang, A self-powered vector motion sensor for smart robotics and personalized medical rehabilitation, Nano Energy 104 (2022), 107936.
[15] Z.L. Wang, Triboelectric nanogenerators as new energy technology and self-powered sensors-principles, problems and perspectives, Faraday Discuss. 176 (2014) 447–458.
[16] F. Fan, Z. Tian, Z.L. Wang, Flexible triboelectric generator!, Nano Energy 1 (2012) 328–334.
[17] S. Mishra, P. Supraja, D. Haranath, R.R. Kumar, S. Pola, Effect of surface and contact points modification on the output performance of triboelectric nanogenerator, Nano Energy (2022), 107964.
[18] J. Wang, X. Yu, D. Zhao, Y. Yu, Q. Gao, T. Cheng, Z.L. Wang, Enhancing output performance of triboelectric nanogenerator via charge clamping, Adv. Energy Mater. 11 (2021), 2101356.
[19] X. Han, J. Niu, Y. Wang, X. Jin, L. Peng, J. Chen, X. Wei, X. Liu, W. Wang, H. Wang, T. Lin, Polyaniline-based Schottky-triboelectric hybrid DC generators with tunable electrical outputs, Nano Energy 104 (2022), 107956.
[20] Z.L. Wang, Triboelectric nanogenerator (TENG)—sparking an energy and sensor revolution, Adv. Energy Mater. 10 (2020), 2000137.
[21] Z. Wu, T. Cheng, Z.L. Wang, Self-powered sensors and systems based on nanogenerators, Sensors 20 (2020) 2925.
[22] Q. Gao, T. Cheng, Z.L. Wang, Triboelectric mechanical sensors-progress and prospects, Extrem. Mech. Lett. 42 (2021), 101100.
[23] C. Wang, X. Zhang, J. Wu, X. Yu, T. Cheng, H. Ma, Z.L. Wang, Double-spring-piece structured triboelectric sensor for broadband vibration monitoring and warning, Mech. Syst. Signal. Pract. 166 (2022), 108429.
[24] Q. Han, Z. Ding, Z. Qin, T. Wang, X. Xu, F. Chu, A triboelectric rolling ball bearing with self-powering and self-sensing capabilities, Nano Energy 67 (2020), 104277.
[25] X. Zhang, Q. Gao, Q. Gao, X. Yu, T. Cheng, Z.L. Wang, Triboelectric rotary motion sensor for industrial-grade speed and angle monitoring, Sensors 21 (2021) 1713.
[26] C. Garcia, I. Trendafilova, J. Sanchez Del Rio, Detection and measurement of impacts in composite structures using a self-powered triboelectric sensor, Nano Energy 56 (2019) 443–453.
[27] Q. Xu, Y. Lu, S. Zhao, N. Hu, Y. Jiang, H. Li, Y. Wang, H. Gao, Y. Li, M. Yuan, L. Chu, J. Li, Y. Xie, A wind vector detecting system based on triboelectric and photoelectric sensors for simultaneously monitoring wind speed and direction, Nano Energy 89 (2021), 106382.
[28] Z. Song, X. Zhang, Z. Wang, T. Ren, W. Long, T. Cheng, Z.L. Wang, Nonintrusion monitoring of droplet motion state via liquid-solid contact electrification, ACS Nano (2021).
[29] P. Kanokpaka, L.-Y. Chang, B.-C. Wang, T.-H. Huang, M.-J. Shih, W.-S. Hung, J.-Y. Lai, K.-C. Ho, M.-H. Yeh, Self-powered molecular imprinted polymers-based triboelectric sensor for noninvasive monitoring lactate levels in human sweat, Nano Energy 100 (2022), 107464.
[30] J. Yang, J. An, Y. Sun, J. Zhang, L. Zu, H. Li, T. Jiang, B. Chen, Z.L. Wang, Transparent self-powered triboelectric sensor based on PVA/PA hydrogel for promoting human-machine interaction in nursing and patient safety, Nano Energy 97 (2022).
[31] X. Yang, G. Liu, Q. Guo, H. Wen, R. Huang, X. Meng, J. Duan, Q. Tang, Triboelectric sensor array for internet of things based smart traffic monitoring and management system, Nano Energy 92 (2022), 106757.
[32] X. Hou, M. Zhu, L. Sun, T. Ding, Z. Huang, Y. Shi, Y. Su, L. Li, T. Chen, C. Lee, Scalable self-attaching/assembling robotic cluster (S2A2RC) system enabled by triboelectric sensors for in-orbit spacecraft application, Nano Energy 93 (2022), 106894.
[33] X. Pu, H. Guo, Q. Tang, J. Chen, L. Feng, G. Liu, X. Wang, Y. Xi, C. Hu, Z.L. Wang, Rotation sensing and gesture control of a robot joint via triboelectric quantization sensor, Nano Energy 54 (2018) 453–460.
[34] Z. Wang, J. An, J. Nie, J. Luo, J. Shao, T. Jiang, B. Chen, W. Tang, Z.L. Wang, A self-powered angle sensor at nanoradian-resolution for robotic arms and personalized medicare, Adv. Mater. 32 (2020), 2001466.
[35] Z. Xie, J. Dong, F. Yang, R. Xu, Q. Gao, T. Cheng, Z.L. Wang, Sweep-type triboelectric linear motion sensor with staggered electrode, Extrem. Mech. Lett. 37 (2020), 100713.
[36] Q. Jing, G. Zhu, W. Wu, P. Bai, Y. Xie, R. Han, Z.L. Wang, Self-powered triboelectric velocity sensor for dual-mode sensing of rectified linear and rotary motions, Nano Energy 10 (2014) 305–312.
[37] H. Guo, J. Chen, Q. Leng, Y. Xi, M. Wang, X. He, C. Hu, Spiral-interdigital-electrode-based multifunctional device: dual-functional triboelectric generator and dual-functional self-powered sensor, Nano Energy 12 (2015) 626–635.